Negative acoustic index metamaterial

L. Fok and X. Zhang*

Nanoscale Science and Engineering Center (SINAM), 3112 Etcheverry Hall, University of California, Berkeley, California 94720, USA

(Received 13 December 2010; revised manuscript received 28 February 2011; published 9 June 2011)

Acoustic metamaterials utilizing periodic deep subwavelength resonators can attain negative acoustic properties unavailable in nature. We have developed a negative acoustic index metamaterial for water that combines Helmholtz and rod-spring resonators to control effective bulk modulus and mass density, respectively. Effective properties extracted from full-wave simulations of our metamaterial show that negative real components of bulk modulus and density occur simultaneously, resulting in a negative real component of the acoustic index. Experimental measurements on a sample of this metamaterial confirm that the real components of the acoustic index and bulk modulus attain negative values, but the density does not become negative. The primary causes of this are identified and potential solutions are presented.

DOI: 10.1103/PhysRevB.83.214304 PACS number(s): 43.20.+g, 43.35.+d

I. INTRODUCTION

Engineered acoustic materials are used to attain properties and phenomena unavailable in nature. Sonic or phononic crystals utilize microstructures with periodic high impedance inclusions in a low impedance matrix. Numerous novel phenomena have been demonstrated using these crystals including focusing, negative refraction, tunneling, and wave guiding.[1–12] Physically, these phenomena are caused by Bragg scattering in an array of unit cells near the first Brillouin-zone edge, when the wavelength in the matrix is comparable to the periodicity. This prohibits effective-medium theory and assignment of effective properties to the materials, and also limits the phenomena to frequency bands in specific directions. Bragg scattering also requires these crystals to be at least several wavelengths thick, which can be impractically large for the frequencies and phase speeds common in acoustics.

Acoustic metamaterials have the potential to achieve unique, unprecedented effective acoustic properties[13–20] while maintaining reasonable sample sizes. Analogous to their electromagnetic counterparts,[21–24] these materials utilize engineered deep subwavelength microstructures, making effective-medium theory and effective properties appropriate. Unprecedented anomalous effective properties have been predicted and demonstrated using these designs, with negative acoustic and elastic properties drawing major interest due to the implications of new interface and shear modes, evanescent wave enhancement, and reversed Doppler effect and refraction. For metamaterial fluids, the two relevant constituent properties are bulk modulus and density. Negative bulk modulus[25,26] and negative density[27–31] have been studied extensively, with the ultimate goal of attaining a negative acoustic index through simultaneous negative bulk modulus and density.[32–36]

Despite this large amount of work, fewer experimental demonstrations of negative acoustic index metamaterials exist. The two works known to the authors are a one-dimensional (1D) air-filled waveguide metamaterial[37] and a 2D water-filled acoustic network metamaterial.[38] Lee *et al*. demonstrated negative phase velocity in a metamaterial formed from short tube segments, each with a side hole to open air, connected in series with a plastic membrane at each junction. This metamaterial design can in principle be generalized to two dimensions for frequencies up to a few kHz in air. Zhang *et al*.'s design consisted of two adjacent half spaces of interconnected water-filled channels and cavities. The half spaces were shown analytically to have opposite effective index signs, which was supported by experimentally observed refocusing of a point source placed in the positive index half space.

We present numerical and experimental evidence of a negative acoustic index in a water-based 2D acoustic metamaterial operating in the 18–22-kHz range. Helmholtz (HH) resonators and rod-spring (RS) resonators are shown to drive effective bulk modulus and density negative over overlapping frequency bands in simulations using realistic properties, resulting in a negative acoustic index over this band. Details of the experimental implementation of our metamaterial and the testing methodology are presented, with special emphasis on the effects of finite material property contrast.

II. THEORETICAL DESIGN AND MODELING

Negative bulk modulus and density in harmonically excited systems correspond to average unit-cell accelerations and deformations that significantly lag the applied stresses in phase. Mechanical resonators provide these phase shifts and the large response amplitudes needed to dominate the unit-cell average. Our unit cell consisted of a RS resonator, shown in Fig. 1(a), and HH resonators, shown in cross section in Fig. 1(b). These resonators are combined into a single unit cell shown in Fig. 1(c), where the RS resonator (middle) is highlighted in red (light gray) and four HH resonators (top and bottom) are highlighted in blue (gray).

RS resonators are a form of mass-spring-damper resonators, which have been shown theoretically[39] and experimentally[27,28] to attain negative density values near resonance in elastic metamaterials. From Newton's second law, a negative real density component requires that the average acceleration of a unit cell lag the applied force by 90°–270°. Mass-spring dampers naturally attain this phase delay above the resonant frequency and also have sufficiently high amplitude around the resonant frequency to dominate the unit-cell average. Our RS resonators used a similar approach in this fluid acoustic metamaterial, with each resonator composed of an aluminum rod acting as the mass connected to poly(methyl methacrylate) (PMMA) discs acting as springs, shown in Fig. 1(a). The springs were hidden in cavities to minimize their scattering of

 ©2011 American Physical Society

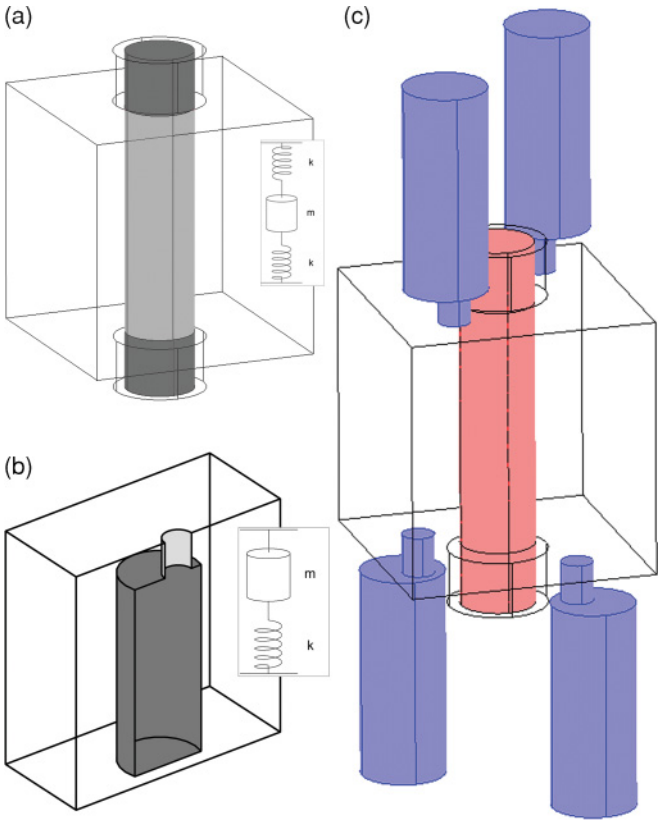

FIG. 1. (Color online) Negative acoustic index metamaterial design. (a) Rod-spring resonator composed of a 3-mm-diameter, 1-cm-long aluminum rod acting as a mass, shaded light gray, connected to the waveguide walls by 3-mm-diameter, 2.5-mm-long PMMA discs acting as shear springs, shaded dark gray. The inset shows the equivalent lumped mechanical model with mass m and two springs with spring constant k. (b) Helmholtz resonator cross section composed of a 1.25-mm-diameter, 1.5-mm-long neck fluid acting as a mass, shaded light gray, and 3-mm-diameter, 8.5-mm-long cavity fluid acting as a spring, shaded dark gray. The inset shows the equivalent lumped mechanical model. (c) Unit cell consisting of a rod-spring resonator, shaded red (light gray) and four Helmholtz resonators shaded blue (gray). Each edge of the wire-frame cube is 1 cm long.

waves passing through the water-filled unit cell and are rigidly attached at their ends to the rod and walls. Since aluminum has a much higher elastic modulus and shear modulus than PMMA, disc shear should be the primary deformation under acoustic excitation. Assuming that only disc shear occurs, a rough estimation of the resonance frequency ω_{RS} is given by

$$\omega_{RS} = \sqrt{\frac{E_s r_s^2}{(1+\nu)\, h_s h_r \rho_r r_r^2}}, \tag{1}$$

where E_s is the spring elastic modulus, r_s is the spring radius, ν is the spring Poisson ratio, h_s is the spring height, h_r is the rod height, ρ_r is the rod density, and r_r is the rod radius. The actual resonance frequency will be lower due to rod deformations, nonshear deformations, and the mass of the surrounding fluid. Adding the fluid density to the rod material density is a first-order correction for the surrounding fluid mass that greatly improves the estimate.

Helmholtz resonators have been previously shown to attain negative effective bulk modulus values in a 1D water-filled waveguide.[25] Attaching HH resonators to a 1D or 2D waveguide with height sufficiently smaller than a half wavelength constrains the directional response and radiation pattern from the neck fluid in free space to the waveguide propagation plane. In this plane, the response and radiation patterns are isotropic, allowing HH resonators to affect the isotropic property bulk modulus. For a HH resonator with deep subwavelength dimensions, rigid walls, and a neck much smaller than the cavity, the resonance frequency ω_0 can be approximated[40] by

$$\omega_0 = c\sqrt{\frac{S}{L'V}}, \tag{2}$$

where $c$is the fluid phase speed, S is the neck cross-section area, V is the cavity volume, and L' is the effective throat length. The effective throat length accounts for the impedance mismatch at the neck exit and is defined as the actual length plus 1.7 times the neck radius. Our unit-cell design shown in Fig. 1(c) utilized four Helmholtz resonators, shown in Fig. 1(b), per unit cell positioned for integration with the RS resonators into a well defined unit cell and to reduce coupling between adjacent HH resonators. A well defined unit cell provides clear boundary positions for a layer of metamaterial, which are needed in the reflection/transmission (RT) effective property extraction routine used here.[41] This RT property extraction method combines complex reflection and transmission coefficients from experiments or simulations with sample dimensions in an analytical relation resulting in effective acoustic index and impedance, from which density and modulus can be calculated.

Coupling here refers to a resonance frequency shift or bandwidth change created by interaction between adjacent resonators through an unintended mechanical link. By using four smaller HH resonators more evenly distributed around the RS resonator with the same resonance frequency as a single larger HH resonator, coupling between HH resonators was decreased in two ways. First, smaller HH resonators have smaller individual response amplitudes, reducing all near-field interactions. Second, spreading the HH resonators to the top and bottom of a unit cell increased the amount of material between the cavities of adjacent resonators, reducing near-field interactions between adjacent cavities. While unimportant in an idealized system with perfectly rigid walls, real HH are formed in an elastic material with finite compressibility, allowing stress field penetration into the walls.

Finally, one commonly neglected issue that must be considered in the analysis of real passive metamaterials are the effects of complex material properties caused by intrinsic material loss, specifically with regard to the claim of negative index. When density and bulk modulus are complex, the acoustic index

$$n = \frac{c_0}{|B|}\sqrt{\rho' B' + \rho'' B'' + i\,(\rho'' B' - \rho' B'')} \tag{3}$$

becomes complex, where n is the refractive index, c_0 is the reference phase speed, B is the bulk modulus, and ρ is the density. Single primes in Eq. (3) denote real components and double primes denote imaginary components. Equation (3)

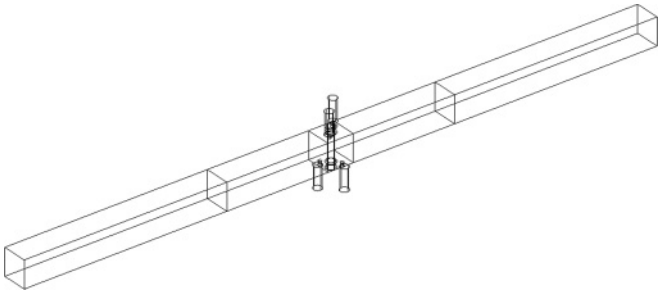

FIG. 2. Simulation domain with unit cell of negative acoustic index metamaterial in center. The outer rectangular prism domains measure 1 cm × 1 cm × 4 cm, the inner rectangular prisms measure 1 cm × 1 cm × 2 cm, and the center cube has 1-cm edge lengths.

shows that a negative real component of the acoustic index can occur under conditions outside the commonly mentioned combination of real and negative bulk modulus and density. In addition, even if a material has negative real components of bulk modulus and density, the imaginary index component magnitude can still be larger than the real component. Imaginary index components in passive metamaterials imply damping of propagating waves and phase distortion of evanescent waves. Since the strength of these effects is dependent on the relative values of index components, both must be known to evaluate a negative acoustic index metamaterial.

We performed finite-element simulations of our negative acoustic index design using COMSOL Multiphysics. The basic simulation domain is shown in Fig. 2. Two water filled lead-in and lead-out segments were placed on each side of the metamaterial layer, with pressure measurements for RT extraction done at the interface between each pair. Varying the measurement plane distance indicated that the near field extended approximately 0.5–1 cm away from the unit-cell edge. With the appropriate phase correction for propagation in water, measurements on planes further away from the metamaterial unit-cell edge, in this case 2 cm, resulted in consistent extracted properties. A 1-Pa-amplitude plane harmonic wave was sent into the domain via a radiation boundary condition at the leftmost boundary face and a zero radiation boundary condition was applied to the rightmost boundary face. Radiation boundary conditions allow user-defined plane waves to enter the domain while absorbing all plane waves incident on the boundary from the simulation domain. These boundaries were 6 cm away from the metamaterial unit-cell edge, which is well outside the near-field region. As a result, the extracted results were not affected by the specific distance chosen. The domain side walls were assigned a zero pressure gradient since the structure repeats in the direction transverse to both the RS axis and propagation direction, and is a rigid waveguide wall in the remaining transverse direction.

Each RS resonator consisted of an aluminum rod 3 mm in diameter and 1 cm long, and two PMMA discs 3 mm in diameter and 2.5 mm tall. Pockets for the PMMA discs were 4 mm in diameter and 2.5 mm tall. The center-line axis of each RS was positioned in the center of a unit cell, 5 mm from each transverse boundary. RS resonator domains were modeled as linear elastic materials using the properties[40,42,43] shown in Table I, which also includes water

TABLE I. Material properties.

Material property	Value
PMMA elastic modulus	4.25 GPa + i*0.15 GPa
PMMA Poisson ratio	0.375
PMMA density	1190 kg/m^3
Aluminum elastic modulus	70 GPa
Aluminum Poisson ratio	0.33
Aluminum density	2700 kg/m^3
Water density	998 kg/m^3
Water sound speed	1481 m/s

properties. Since PMMA property values vary moderately from sample to sample, we selected values within the typical range that resulted in a resonance frequency roughly matching preliminary experiments on samples with RS resonators alone. The estimated resonance frequency using these properties and dimensions in Eq. (1) with the water density added to the rod density is 29 kHz.

Each HH resonator consisted of a cylindrical cavity 3.4 mm in diameter and 8.5 mm long connected to the unit cell through a cylindrical neck 1.25 mm in diameter and 1.5 mm long. The estimated resonance frequency using these dimensions in Eq. (2) is 21 kHz. The neck center-line axes were 2.5 mm offset in both transverse directions from the RS resonator center-line axis, while the cavity center-line axes were offset 3 mm in both transverse directions from the RS center-line axis. Larger cavity offsets were selected to provide extra material between the HH cavities and spring pocket for machining errors. Small amounts of loss were added to the neck (8%) and cavity (4%) to mimic viscous losses and the effect of elastic walls. The percentage refers to the magnitude of the imaginary sound speed component relative to the magnitude of the complex sound speed.

The effective bulk modulus and density components extracted from simulations of this metamaterial using the RT method mentioned earlier are shown in Fig. 3, and the acoustic index components are shown in Fig. 4. To verify that the selected metamaterial boundaries were correct, simulations of layers 1–4 unit cells thick were performed.[41] Identical properties within numerical error were obtained from these simulations, verifying that the boundary position locations were correct. The real components of bulk modulus and mass density are simultaneously negative from 19 to 20 kHz, resulting in negative real component of acoustic index values over the same frequency band. Using the midpoint between the peak and minimum values of real bulk modulus or density as a guide, the actual HH resonance frequency is about 21 kHz and the actual RS resonance frequency is about 19 kHz. Compared to the frequencies estimated using Eqs. (1) and (2), the HH frequency estimate is fairly accurate while the RS estimate is significantly higher than reality. Displacement cross sections showed that the primary cause deviation from Eq. (1) in this design was rod deformation. Varying the intrinsic loss in the PMMA and HH sections had the intuitively expected effects. Decreased loss maintained the general curve shapes, but increased the ratio of real to imaginary index component magnitudes in the negative region and widened the frequency band with a negative acoustic

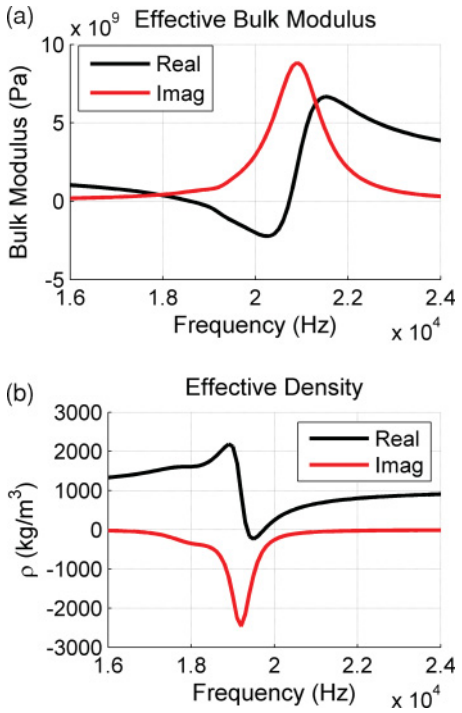

FIG. 3. (Color online) Effective (a) bulk modulus and (b) density of our simulated negative acoustic index unit cell. Real components are shown in black and imaginary components in red (gray).

index. Naturally, experimental results will be different due to variations in machining quality, actual material properties/loss, and practical experiment issues.

III. EXPERIMENTAL CHARACTERIZATIONS

During the process of creating an experimental system to test our metamaterial, we encountered major problems in water-filled waveguides constructed from real materials with finite dimensions over the 15–25-kHz range. Pulse transmission measurements in a 1-cm × 1-cm-square cross-section aluminum waveguide with 10-mm-thick walls revealed the existence of an additional hybrid metal-fluid mode, shown in Fig. 5(a) for 20 kHz, and strong dispersion in the planar water mode, shown in Fig. 5(b). Similar results were obtained for lower frequencies using shorter pulses. Subsequent numerical eigenmode analysis of finite cross-section waveguides with elastic walls indicated that these effects could not be made sufficiently weak for RT property extraction using reasonable dimensions for our facilities.

We elected to use multirow samples such as the negative acoustic index sample shown in Fig. 6 and test them in the anechoic chamber shown in Fig. 7 to avoid waveguide issues. Each sample consisted of six stainless-steel bars 1 cm × 1 cm × 11 cm that form the sample support structure, with the HH resonators and pockets for the PMMA discs machined in the center 7 cm of each bar. Adjacent HH bars were sealed with tape then glued together using marine epoxy. Once the epoxy was cured, RS resonators were assembled and attached to the bars using superglue. Finally, to prevent sample breakage during handling, additional bars 1 cm × 1 cm × 3 cm were screwed on to the sides with a buffer layer of marine epoxy,

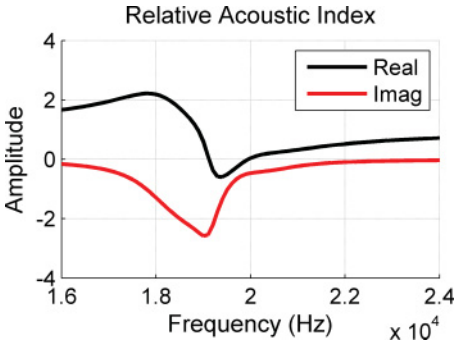

FIG. 4. (Color online) Effective acoustic index of simulated negative acoustic index metamaterial unit cell relative to water. Real components are shown in black and imaginary components in red (gray).

connecting the ends of bar pairs surrounding each rod-spring row. The resultant samples had three rows of seven unit cells, equaling a cross section approximately one wavelength (λ) by one wavelength at 20 kHz.

Changing to multirow samples resolved the issue of waveguide use by including the support structure containing the HH in the unit cell of this design, which is a 1-cm × 1-cm × 3-cm rectangular prism. Effective properties extracted from simulations of this new unit cell modeling the stainless bars as elastic media showed that simultaneous negative real components of the acoustic index, bulk modulus, and density can still occur with similar frequency dependencies as in Figs. 3 and 4. However, tolerance of intrinsic material loss is reduced, which can be understood by viewing the new unit cell as a composite of negative and positive acoustic index blocks. A homogenization of the three blocks can still be negative, provided that the negative properties are sufficiently strong to dominate the average.

Experimental measurements of the reflection and transmission coefficients of these samples were done in the rectangular anechoic cavity constructed from Syntech Materials Inc. SADM-1 absorbing panels, shown in Fig. 7. SADM-1 is a commercially available echo-reduction acoustic material designed for water operation in the 10–100-kHz frequency range. The cavity dimensions were roughly 24 cm × 24 cm × 75 cm, which is equivalent to 3.25λ × 3.25λ × 10.3λ in water at 20 kHz. Pulse-echo measurements indicated that the reflected wave amplitude was less than 10% of the incoming wave within the frequency range of interest, good anechoic chamber performance.

To create plane waves for RT measurements, we collimated spherical waves generated by a Reson Inc. TC-4033 spherical transducer driven by a Stanford Research Systems DS345 function generator using a custom-made Nylon 6/6 lens. This lens/transducer combination was chosen due to the impractically large source that would be needed to directly create plane waves in the target frequency range. The 6–in. x 6–in. cross-section Nylon 6/6 lens was double-concave with 17.65-cm radii of curvature, with a target source distance of 25 cm. Experimental measurements found a flat phase front beam at least 5 cm × 5 cm in cross section was created from 15 to 20 kHz, after which both amplitude and phase distortions rapidly grew with rising frequency. These and other pressure

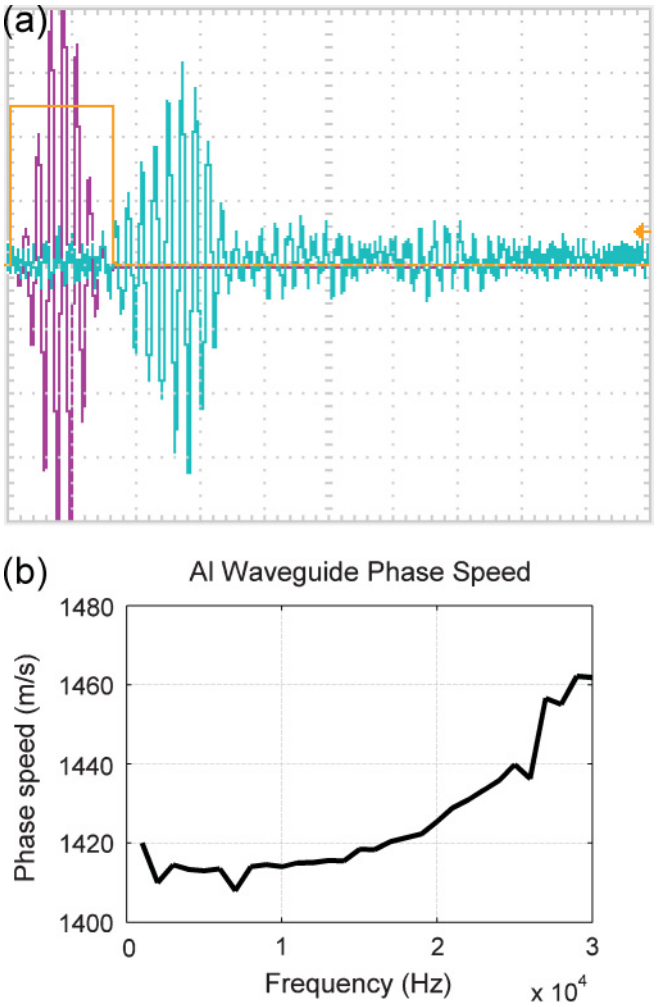

FIG. 5. (Color online) Aluminum waveguide pulse experiment results. (a) Oscilloscope trace of driving voltage in magenta (dark gray) and hydrophone signal in teal (light gray) at 20 kHz. The later portion of the hybrid mode and early portion of the water mode overlap and constructively interfere in this case. (b) Phase speed of water mode inside the waveguide.

signals were measured using Reson TC-4013 hydrophones mounted on a rail system for positioning accuracy and repeatability. Hydrophone signals were passed through a Reson VP2000 amplifier, providing very low noise 50-dB power amplification and bandpass filtering, recorded using a Tektronics TDS2004B digital oscilloscope, then downloaded to a computer for processing.

Each sample test consisted of measuring the pressure under continuous-wave excitation 2 cm from the leading and trailing sample faces, then in the same positions without the sample. This distance was just beyond the near field of the samples according to simulations. At each position, snapshots of the hydrophone and driving signals were recorded for a set of frequencies, with a pause of 3 sec following frequency changes to allow for steady state. Continuous-wave excitation avoided transient effects from resonators but increased effects from imperfect absorbing boundary conditions and reflections among the various objects in the chamber. These noise sources were reduced by averaging reflection and transmission coefficients

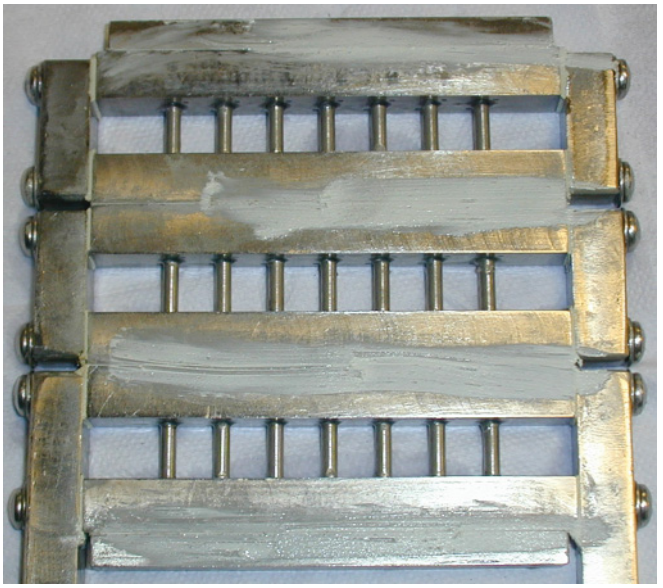

FIG. 6. (Color online) Negative acoustic index metamaterial sample. The RS resonator rods are visible, while the HH are formed in the horizontal stainless-steel bars leaving only the neck openings visible.

from measurements with the sample at five different positions in the cavity.

IV. EXPERIMENTAL RESULTS AND DISCUSSION

Prior to performing experiments on negative acoustic index samples, the existence of unintended resonances and interactions due to the finite sample dimensions and structure was tested using a sample without resonators. The measured transmission coefficients amplitudes with this sample at five different positions in the cavity and the average are shown in Fig. 8. No major resonances appear in the average, supporting the belief that the HH and RS resonators in negative acoustic index samples were responsible for the anomalous properties. The transmission curves for individual sample positions do show the existence of various weak, position dependent modes. These were likely the undesired modes caused by reflection

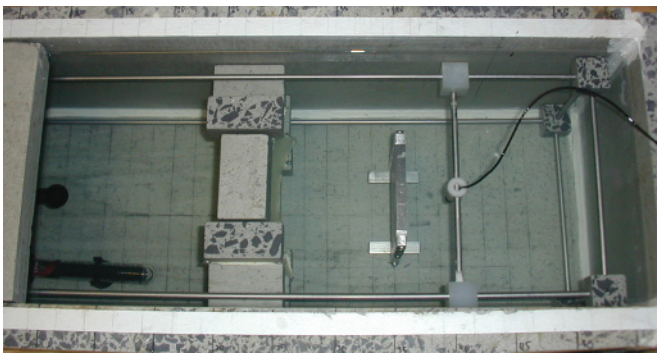

FIG. 7. (Color online) Experimental test bay with cover removed. The spherical source and heater can be seen on the left, lens left of center, sample right of center, and receiver on the right of the sample. The metal rail frame and guidelines drawn on the bottom assisted in object and sensor positioning.

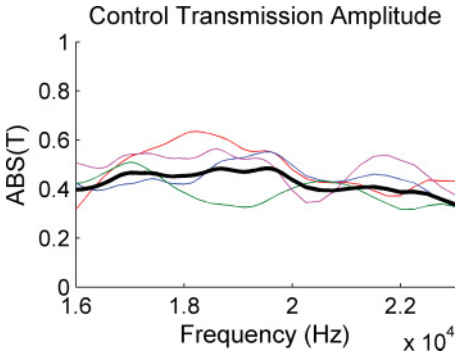

FIG. 8. (Color online) Transmission coefficient amplitude for a control sample at multiple positions. Thin color (gray) lines are measurements with the sample at different positions, while the thick black line is the average.

between objects in the cavity and imperfect boundary absorption, and were successfully reduced by averaging the results at multiple positions.

The effective properties from our best-performing negative acoustic index sample are shown in Fig. 9. The real part of the acoustic index, marked in red (gray), is negative in the frequency band 19–20 kHz, as desired, but a jump occurs above 20 kHz that is discussed shortly. The resonance induced dips in density and bulk modulus also occur over this band, with the real component curve shapes approximately matching simulation outside of a small feature around 18 kHz. However, while the real bulk modulus component attains negative values, the real density component does not go negative. As noted earlier in Eq. (3), this does not prohibit the existence of a negative real component of the acoustic index since bulk modulus and density are complex properties. However, large imaginary modulus and density components may result in a large imaginary acoustic index component, which was the case here.

While these results indicate that our metamaterial attained a negative real acoustic index, several important issues must be addressed, beginning with the jump in effective index. The large jumps in the real and imaginary index components above 20 kHz were triggered by the RT extraction routine requiring a positive real component of impedance and negative imaginary component of refractive index. These are required of passive metamaterials since the combined reflected and transmitted wave powers cannot exceed the incoming power. However, when one or both of these components is close to zero, as occurred in our case, measurement errors and deviations in assumed values can prevent the existence of a solution meeting both requirements. It is important to note that these jumps are different from the branch jumps mentioned in Ref. 41. Those branch jumps are caused by the existence of other material property sets that satisfy the passive metamaterial requirements and correspond to the same RT coefficients. Each branch corresponds to a different number of complete effective wavelengths inside a layer of metamaterial and can be avoided through appropriate frequency scanning parameters. In this case, the effective wavelength in the sample remained significantly larger than the sample itself.

Quantitatively, the experimental HH resonator performance greatly exceeded expectations, attaining a peak negative

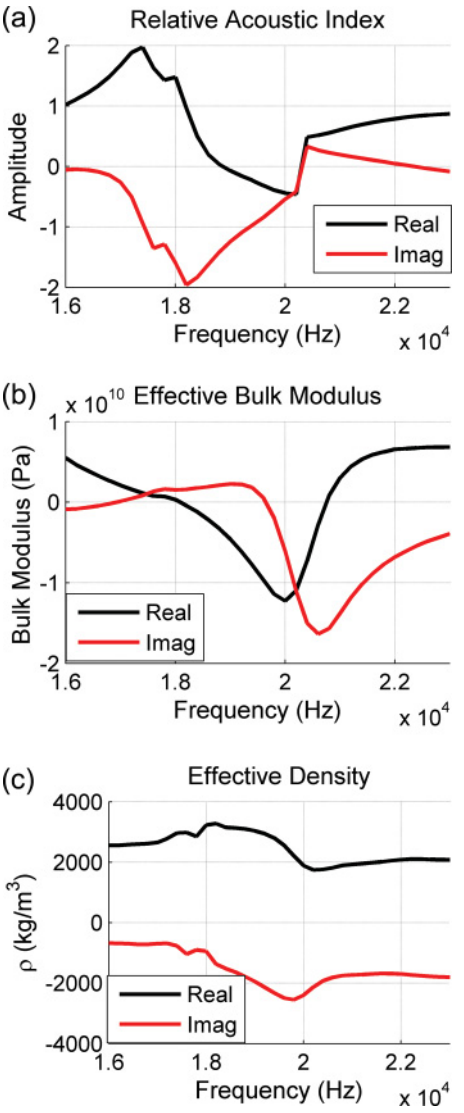

FIG. 9. (Color online) Effective properties of best experimental sample. (a) Effective acoustic index relative to the surrounding water. (b) Effective bulk modulus. (c) Effective density.

modulus almost an order of magnitude greater than the ideal waveguide simulation. Much lower actual intrinsic losses were likely responsible for this performance, which also explains the resonance feature in density at 18 kHz. HH resonators alone can be shown in simulations to cause a small resonance feature in effective density at a frequency below the bulk modulus resonance when loss is sufficiently low. RS resonators, on the other hand, were unable to attain sufficiently large response amplitudes to drive the real component of density negative in any sample. The lowest attained value in this sample was approximately 2000 kg/m^3, and the lowest attained value throughout all tested samples that attained a negative real component of index was approximately 1000 kg/m^3.

As a result of this insufficient RS resonator performance, a comparison of the real and imaginary acoustic index components indicates that although this design achieved the goal of a negative acoustic index, its usefulness will be very limited. The imaginary index component magnitude is significantly larger than the magnitude of the real component

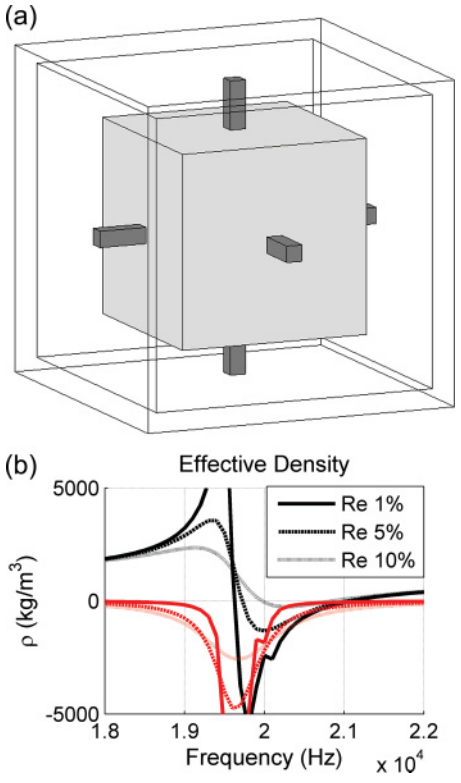

FIG. 10. (Color online) 3D negative density resonator. (a) Unit cell composed of the lead core, shaded in light gray, lead pin fins, shaded in dark gray, and cubic aluminum shell is shown in wireframe. (b) Effective density as a function of frequency for various loss factors. The imaginary components for each loss factor are plotted in red (gray) with the corresponding line type.

over the entire negative acoustic index band prior to the jump, ruling out observation of interesting phenomena in propagating and evanescent waves outside of extraordinary damping. This is analogous to earlier electromagnetic negative index metamaterial where a negative real index component was realized by single negative and large imaginary components of permittivity and permeability.[44]

Insufficient RS resonator response to drive the density negative can likely be attributed to intrinsic loss in the PMMA springs combined with the experimental sample design. PMMA was selected for its low intrinsic loss relative to most polymers. However, polymers have strongly frequency-dependent properties and may be sensitive to moisture, leading to higher loss than expected. Unfortunately, we were unable to test this theory due to the lack of a shear modulus testing apparatus capable operation in the 15–25-kHz frequency band. The effect of intrinsic loss was amplified by utilization of a multirow sample to overcome undesired waveguide induced dispersion. As noted earlier, the unit cell can be viewed as a composite of positive and negative materials, which increases the necessary RS and HH resonator response amplitudes to drive the total average associated properties negative.

Two possible methods to mitigate the effects of the structure are utilizing impedance matching horns and combining the adjacent HH rows into a single bar. Properly designed impedance matching horns reduce the structure effects by channeling energy into and out of the resonator region with minimal reflection over a frequency band. The primary challenge with these horns is developing a property extraction method for the three-layer horn-metamaterial-horn system, with the horn properties dispersive but known. Combining adjacent HH rows into a single bar would directly reduce the volume filling ratio of positive to negative materials. Fabrication difficulty is the primary challenge for this method, with the possibility of other undesired modes an additional potential problem arising from the decreased structure mass.

The rapid decline in lens performance at frequencies above 20 kHz is partly to blame for the generation of sufficient experimental error to cause jumps in the extracted acoustic index. Two factors responsible for this were approximations made in the lens design and intrinsic polymer loss. The accuracy of the lensmaker's equation with the thin lens approximation used to determine the lens geometry declines with increasing frequency, leading to distortion in the phase front. Increased intrinsic polymer loss with rising frequency increases the difference in damping for rays traveling through different sections of the lens, further distorting phase fronts. Other known sources of error in these experiments were the finite beam and sample size and scattering off other objects in the anechoic chamber. Finite beam and sample size generate distortion via uneven excitation, refraction around the sample, and noise from sound reflected off the walls and around the sample. These can be avoided by utilizing a larger test facility and sample. However, scattering from objects besides the sample in the anechoic chamber can never be totally avoided, since the transducers and receivers themselves scatter waves. This scattering increases with frequency, as the size of the objects relative to the wavelength increases with frequency.

Even with improved experimental facilities and fabrication, loss remains the largest obstacle to negative acoustic index metamaterials. Two possible methods to mitigate this issue are designing loss tolerant resonators for passive metamaterials and using active elements in metamaterials. Active acoustic metamaterials are currently in the early stages of theoretical development and are outside the scope of this work. Recently, several works have been published covering the use of piezoelectric elements to manipulate bulk modulus and density.[45–47] We designed a highly loss tolerant density resonator shown in Fig. 10(a). This resonator is composed of a high mass 3-mm edge length cubic lead core connected to a low mass 5-mm outer edge length cubic aluminum shell through six thin 250-μm $\times$ 250-μm $\times$ 750-μm lead pin fins that act as springs. Due to the large mass contrast, the lead core acts as an inertial anchor about which the aluminum shell oscillates, reducing the design to a mass-spring-damper oscillator. The key feature of this design is that the springs are formed from a minimal amount of material. This decreases the total volumetric deformation required to achieve the same shell displacement and also allows the use of a wider range of materials for the springs. To demonstrate the increased loss tolerance, simulations were performed with the resonator placed at the center of a water-filled cube with 1-cm edge lengths, similar to Fig. 2. The effective density for several loss factors is shown in Fig. 10(b). In reality, gravity would require the resonators to be suspended in a gel matrix with properties similar to water and minimal support of shear modes. This gel matrix would also support the inclusion of an array of stable

gas filled voids (bubbles) to act as the bulk modulus resonators to complete the negative index design.

V. CONCLUSION

Theoretical and experimental investigations on an acoustic negative index metamaterial combining Helmholtz and rod-spring resonators was presented. Negative real components of the acoustic index were predicted in simulations and found to occur in the experimental implementation over a narrow frequency band of 19–20 kHz. However, the RS resonator was unable to drive the real part of effective density negative, which we believe is largely due to material loss. Numerical investigations showed that these can be overcome in principle by using improved resonators and active acoustic elements.

ACKNOWLEDGMENTS

L.F. and X.Z. acknowledge support from the U.S. Office of Naval Research (Grant No. N00014-07-1-0626).

*Author to whom correspondence should be addressed. xiang@berkeley.edu

[1] M. S. Kushwaha, P. Halevi, G. Martínez, L. Dobrzynski, and B. Djafari-Rouhani, Phys. Rev. B **49**, 2313 (1994).
[2] S. Yang, J. H. Page, Z. Liu, M. L. Cowan, C. T. Chan, and P. Sheng, Phys. Rev. Lett. **88**, 104301 (2002).
[3] Z. Liu, C. T. Chan, and Ping Sheng, Phys. Rev. B **65**, 165116 (2002).
[4] C. Luo, S. G. Johnson, J. D. Joannopoulos, and J. B. Pendry, Phys. Rev. B **65**, 201104 (2002).
[5] X. Zhang and Z. Liu, Appl. Phys. Lett. **85**, 341 (2004).
[6] S. Yang, J. H. Page, Z. Liu, M. L. Cowan, C. T. Chan, and P. Sheng, Phys. Rev. Lett. **93**, 024301 (2004).
[7] C. Qiu, X. Zhang, and Z. Liu, Phys. Rev. B **71**, 054302 (2005).
[8] X. Hu, C. T. Chan, and J. Zi, Phys. Rev. E **71**, 055601 (2005).
[9] L. Feng, X.-P. Liu, Y.-B. Chen, Z.-P. Huang, Y.-W. Mao, Y.-F. Chen, J. Zi, and Y.-Y. Zhu, Phys. Rev. B **72**, 033108 (2005).
[10] L. Feng, X.-P. Liu, M.-H. Lu, Y.-B. Chen, Y.-F. Chen, Y.-W. Mao, J. Zi, Y.-Y. Zhu, S.-N. Zhu, and N.-B. Ming, Phys. Rev. B **73**, 193101 (2006).
[11] A. Bazan, M. Torres, F. R. Montero de Espinosa, R. Quintero-Torres, and J. L. Aragón, Appl. Phys. Lett. **90**, 094101 (2007).
[12] L.-Y. Wu, W.-P. Yang, and L.-W. Chen, Phys. Lett. A **372**, 2701 (2008).
[13] P. Sheng, *Introduction to Wave Scattering, Localization and Mesoscopic Phenomena*, 2nd ed. (Springer, Heidelberg, 2006).
[14] P. Chaturvedi, K.-H. Hsu, S. Zhang, and N. Fang, MRS Bull. **33**, 915 (2008).
[15] L. Fok, M. Ambati, and X. Zhang, MRS Bull. **33**, 931 (2008).
[16] M.-H. Lu, L. Feng, and Y.-F. Chen, Mater. Today **12**, 34 (2009).
[17] H. Chen and C. T. Chan, J. Phys. D **43**, 113001 (2010).
[18] M. Ambati, N. Fang, C. Sun, and X. Zhang, Phys. Rev. B **75**, 195447 (2007).
[19] X. Ao and C.T. Chan, Phys. Rev. E **77**, 025601 (2008).
[20] M. Ambati, L. Fok, and X. Zhang (unpublished).
[21] J. B. Pendry, Phys. Rev. Lett. **85**, 3966 (2000).
[22] D. R. Smith, W. J. Padilla, D. C. Vier, S. C. Nemat-Nasser, and S. Schultz, Phys. Rev. Lett. **84**, 4184 (2000).
[23] N. Fang, H. Lee, C. Sun, and X. Zhang, Science **308**, 534 (2005).
[24] T. J. Yen, W. J. Padilla, N. Fang, D. C. Vier, D. R. Smith, J. B. Pendry, D. N. Basov, and X. Zhang, Science **303**, 1494 (2004).
[25] N. Fang, D. Xi, J. Xu, M. Ambati, W. Srituravanich, C. Sun, and X. Zhang, Nat. Mater. **5**, 452 (2006).
[26] S. H. Lee, C. M. Park, Y. M Seo, Z. G. Wang, and C. K. Kim, J. Phys.: Condens. Matter **21**, 175704 (2009).
[27] Z. Liu, X. Zhang, Y. Mao, Y. Y. Zhu, Z. Yang, C. T. Chan, and P. Sheng, Science **289**, 1734 (2000).
[28] Z. Liu, C. T. Chan, and P. Sheng, Phys. Rev. B **71**, 014103 (2005).
[29] J. Mei, Z. Liu, W. Wen, and P. Sheng, Phys. Rev. Lett. **96**, 024301 (2006).
[30] Z. Yang, J. Mei, M. Yang, N. H. Chan, and P. Sheng, Phys. Rev. Lett. **101**, 204301 (2008).
[31] S. H. Lee, C. M. Park, Y. M. Seo, Z. G. Wang, and C. K. Kim, Phys. Lett. A **373**, 4464 (2009).
[32] J. Li and C.T. Chan, Phys. Rev. E **70**, 055602 (2004).
[33] J. Li, Z. Liu, and C. Qiu, Phys. Rev. B **73**, 054302 (2006).
[34] Y. Ding, Z. Liu, C. Qiu, and J. Shi, Phys. Rev. Lett. **99**, 093904 (2007).
[35] Y. Cheng, J. Y. Xu, and X. J. Liu, Phys. Rev. B **77**, 045134 (2008).
[36] K. Deng, Y. Ding, Z. He, H. Zhao, J. Shi, and Z. Liu, J. Appl. Phys. **105**, 124909 (2009).
[37] S. H. Lee, C. M. Park, Y. M. Seo, Z. G. Wang, and C. K. Kim, Phys. Rev. Lett. **104**, 054301 (2010).
[38] S. Zhang, L. Yin, and N. Fang, Phys. Rev. Lett. **102**, 194301 (2009).
[39] G. W. Milton and J. R. Willis, Proc. R. Soc. London, Ser. A **463**, 855 (2007).
[40] L. E. Kinsler, A. R. Frey, A. B. Coppens, and J. V. Sanders, *Fundamentals of Acoustics*, 4th ed. (Wiley, New York, 2000).
[41] V. Fokin, M. Ambati, C. Sun, and X. Zhang, Phys. Rev. B **76**, 144302 (2007).
[42] S. Mousavi, D. F. Nicolas, and B. Lundberg, J. Sound Vib. **277**, 971 (2004).
[43] Y. Liao and V. Wells, J. Sound Vib. **295**, 165 (2006).
[44] V. M. Shalaev, W. Cai, U. K. Chettiar, H.-K. Yuan, A. K. Sharychev, V. P. Drachev, and A. V. Kildishev, Opt. Lett. **30**, 3356 (2005).
[45] A. Baz, New J. Phys. **11**, 123010 (2009).
[46] W. Akl and A. Baz, J. Intell. Mater. Syst. Struct. **21**, 541 (2010).
[47] L. R. Fok, Ph.D. dissertation, University of California, Berkeley, 2010.